Two-Dimensional Simulation of Polysilicon Etching with Chlorine in a High Density Plasma Reactor

Dimitris P. Lymberopoulos and Demetre J. Economou

***Abstract*—A two-dimensional fluid simulation of polysilicon etching with chlorine in an inductively-coupled high density plasma source is presented. A modular approach was used to couple in a self-consistent manner the disparate time scales of plasma and neutral species transport. This way, complex plasma chemical reactions (involving electrons, ions and neutrals) as well as surface chemistry can be included in the simulation. The power deposited into the plasma was calculated by an electromagnetics module which solves Maxwell's equations. The power deposition was used in the electron energy module to find the electron temperature and the rate coefficients of electron-impact reactions. These were in turn used as source terms in separate neutral and charged species transport modules. By iterating among the modules, a self-consistent solution was obtained. Quantities of interest, such as power deposition, species density and flux, and etch rate and uniformity were thus calculated. As power deposition was increased, the electron density increased linearly, the plasma became less electronegative, the degree of gas dissociation increased, and the plasma potential remained constant. The radial uniformity of the Cl atom flux was better than that of the ion flux. The reactivity of the wafer as compared to that of the surrounding electrode surface significantly affected the etch uniformity, despite the low pressure of 10 mtorr.**

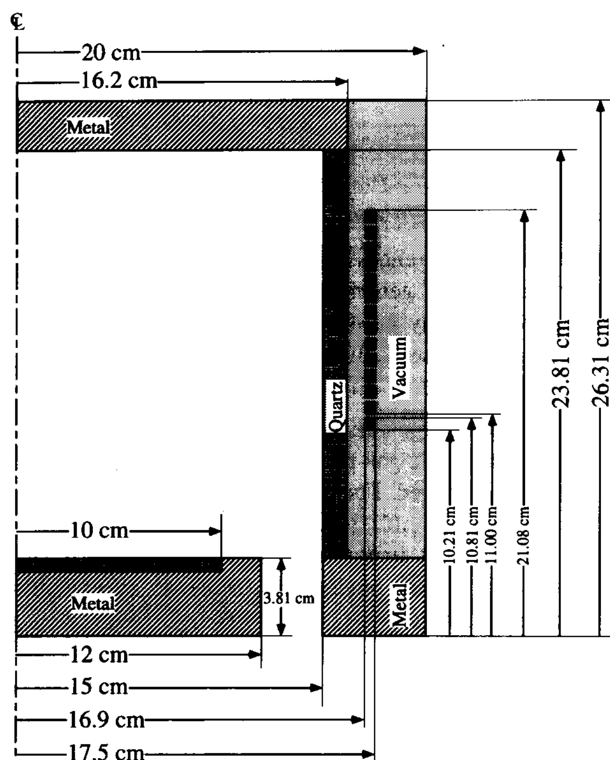

Fig. 1. Design and dimensions of the inductively coupled plasma reactor studied. Due to the axisymmetric nature of the problem only half of the reactor is shown.

I. Introduction

The drive for delineating finer features over larger diameter wafers has resulted in the development of high density plasma (HDP) sources [1]. These reactors operate at low gas pressures (<50 mtorr) to improve uniformity and reduce contamination, and high plasma density ($>10^{11}$ cm^{-3}) to deliver a high flux of ions and radicals to the wafer surface, thereby maintaining a high throughput. Also, low pressure helps anisotropy since the ion mean free path is greater than the sheath dimensions, making ion flow to the wafer directional.

Fig. 1 shows a schematic of the so-called inductively coupled plasma (ICP) source. It can generate a HDP in an azimuthally symmetric chamber bounded by a quartz cylinder and a top metal plate. The plasma is generated by a coil driven at radio frequencies, for example 13.56 MHz. A time-varying axial magnetic field induces an azimuthal electric field which imparts energy to the electrons to sustain the plasma. The electromagnetic wave is absorbed within the skin depth which is a function of plasma density. For typical plasma densities the wave penetrates a few cm from the quartz cylinder wall into the plasma. The power is deposited nonuniformly in the shape of a toroid. Because of the low pressure, however, diffusion is facile and the plasma fills the whole reactor. One of the main goals is to achieve radial plasma and neutral flux uniformity over large diameter (>200 mm) wafers. The wafer platen can be biased independently by a separate RF power supply in order to control the energy of ions bombarding the wafer.

A distinct characteristic of the HDP sources is that the plasma is generated independently of the voltage applied to the substrate electrode. In capacitively-coupled systems, in order to increase the power delivered to the reactor one needs to increase the voltage applied between the electrodes. However, most of the voltage drop in these systems occurs in the sheath next to the electrodes; hence a large fraction of the power is consumed for accelerating ions in the sheath rather than creating radicals and ions in the bulk plasma. In addition, high energy ion bombardment can result in radiation damage and sputtering of the electrodes which in turn leads to device contamination.

Manuscript received Sept. 22, 1994; revised Dec. 21, 1994. This work was supported in part by Sandia National Laboratories under a CRADA with SEMATECH and in part by the National Science Foundation under contract CTS-9216023.

The authors are with the Plasma Processing Laboratory, Department of Chemical Engineering, University of Houston, Houston, TX 77204-4792 USA.

IEEE Log Number 9412956.

0093-3813/95$04.00 © 1995 IEEE

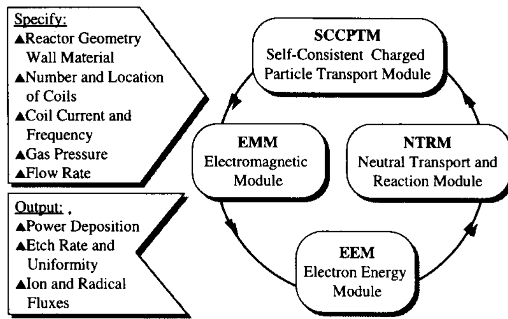

Fig. 2. Modular approach used to couple the disparate time scales of plasma and neutral transport. Important problem inputs and outputs are also shown.

A. High-Density Low-Pressure versus Low-Density High-Pressure

Because of differences in the operating conditions and the way the plasma is generated, the chemistry in high density plasma sources may be different when compared to the relatively high pressure (>100 mtorr) low-density ($\sim 10^9$–10^{10} cm^{-3}) systems. Some differences are

1) Surface chemical reactions of radicals and ions are more important than gas-phase reactions as the operating pressure is lowered. For example, volume recombination is usually negligible below $\sim$ 100 mtorr. Therefore, it is imperative to understand surface chemistry, especially the ion-surface interactions, more so in low pressure HDP systems.
2) Because volume recombination is not efficient, and the wall materials are chosen to minimize wall recombination, the feedstock gas may be highly dissociated. Hence, radical chemistry may dominate over chemistry of the molecules. Correspondingly, the cross-sections of electron impact reactions with radicals (which are difficult to measure) become more important.
3) If the gas is highly dissociated in atoms, and since negative ions usually form by dissociative electron attachment with molecules, the negative ion density in HDP is expected to be much lower than in the high pressure systems. For example, in a high pressure chlorine discharge, negative ions outnumber electrons by more than a hundred times. In a HDP chlorine discharge, the negative ion density may be comparable to the electron density.
4) Because of the high ion flux delivered to the wafer surface, reactive ions may be the primary reactants (the term reactive ion etching, RIE, that is a misnomer when used for traditional high pressure plasma reactors may not be so in HDP sources!)
5) At the low operating pressures of HDP sources, the reaction rate may be limited by reactant supply. For example, to etch a 200 mm-diameter silicon wafer at 1 μ/min with $SiCl_2$ as the etch product, one needs 58 sccm of Cl_2. To maintain a pressure of 1 mtorr with twice that flow rate one needs an *effective* pumping speed of $\sim$ 1500 l/s, i.e., a large pump, accounting for conductance losses. Since the feedstock gas "conversion" (or utilization) may be high, it comes as no surprise the fact that the silicon etch rate can be increased by increasing the gas flow rate [2].

In order to investigate the factors that control gas dissociation and plasma uniformity in HDP sources, we have developed a two-dimensional mathematical model based on the fluid approximation. Other two-dimensional ICP reactor models reported so far include fluid models of an inert (argon) discharge [3], [4], and a hybrid fluid-kinetic model of mixed-gas (Cl_2/Ar) plasmas in an ICP reactor with stovetop coil [5]. In the present work, we report etching of polysilicon with pure chlorine in an ICP reactor with a solenoidal coil. Initial results were reported in [6].

II. Description of the Model

Simulations have been performed for the ICP reactor shown schematically in Fig. 1. Capacitive coupling from the coil can occur, but it is not accounted for in the present paper. Also, the substrate was assumed to be grounded. The species mean free path for the pressure examined (10 mtorr) is $\lambda \sim 1$ cm, while the reactor dimension is $L \sim 10$ cm; this yields a Knudsen number of $Kn = \lambda/L = 0.1$ which is in the transition regime. However, there is evidence that the fluid approximation may be applicable at this or even higher values of Kn [7]. Detailed comparisons with particle (e.g., DSMC) simulations and especially with experiments are necessary to determine how low in pressure the fluid approximation can be used.

The two-dimensional ICP reactor model follows a modular approach similar to that used for capacitively-coupled reactors [8], [9]. The added feature is an electromagnetics (EM) module to calculate the self-consistent power deposited into the plasma by the coil (Fig. 2). The simulation begins by solving Maxwell's equations to determine the electromagnetic fields and power deposition for a specified coil current. The power deposition profile is used as input to the electron energy equation to calculate the electron "temperature" and hence the rate coefficients for electron-impact reactions. In turn these are used in the "source" terms of the neutral and charged species modules. The former is used to calculate the neutral gas composition. The latter is used to calculate the charged particle densities and the self-consistent electrostatic fields. The calculation is repeated in a cyclic fashion until "convergence." From the converged solution, the self-consistent power deposition, electrostatic potential, electron temperature, charged and neutral species densities and flux, etch rate, and uniformity along the wafer radius can be calculated.

A. The Electromagnetics Module

The electromagnetic fields due to the antenna coil are obtained by solving Maxwell's equations in terms of the magnetic vector potential, **A**. For the problem at hand only the azimuthal component of **A** need be computed. The equation solved in this module is

$$\frac{1}{r}\frac{\partial}{\partial r}\left(r\frac{\partial \tilde{A}}{\partial_r}\right)+\frac{\partial^2 \tilde{A}}{\partial z}+\left[\omega^2\mu\varepsilon - r^{-2}\right]\tilde{A} = -\mu\tilde{J} \quad (1)$$

where all quantities are written by their phasor representation ($A_\vartheta = \tilde{A}e^{j\omega t}$, $J_\vartheta = \tilde{J}e^{j\omega t}$). $\tilde{A}$ is the complex amplitude of the magnetic vector potential, ω is the frequency, μ is the permeability of the medium, ε is the (generally complex) dielectric constant of the medium, and $\tilde{J}$ is the current density.

Equation (1) was discretized in space by using the Galerkin finite element method. $\tilde{A}$ was solved for in its complex form. The fields were obtained for the whole domain shown in Fig. 1, but only the plasma zone solution was used in subsequent calculations. Knowing the total current, a current density was specified in the coils; $\mathrm{Re}(\tilde{J})$ was set equal to that current density whereas $\mathrm{Im}(\tilde{J})$ was set equal to zero. $\tilde{A}$ was set to zero all along the conducting boundaries and, by symmetry, at $r = 0$. Once $\tilde{A}$ is computed, the azimuthal electric field is found by

$$E_\vartheta = \mathrm{Re}\,(-j\omega\tilde{A}e^{j\omega t}) \tag{2}$$

and the time-average power deposited into the plasma is given by

$$\mathcal{P} = \tfrac{1}{2}\,\mathrm{Re}\,(\sigma_p|\tilde{E}_\vartheta|^2). \tag{3}$$

Here, the complex plasma conductivityσ_p is given by

$$\sigma_p = \frac{n_e e^2}{m_e(\nu_e + j\omega)} \tag{4}$$

where m_e and ν_e are the electron mass and *effective* momentum-transfer collision frequency, respectively. The plasma dielectric constant ε_p is obtained from

$$\varepsilon_p = \varepsilon_o - j\,\frac{\sigma_p}{\omega} \tag{5}$$

where ε_o is the permittivity of vacuum.

The advantage of solving Maxwell's equation for the whole reactor structure (i.e., including the reactor walls as well as the plasma) is the ability to predict the fraction of the coil power that is dissipated in the reactor walls. For properly designed reactors this fraction should be small. Noncollisional electron heating can be accounted for by using an effective electron collision frequency in (4).

B. Electron Energy Module

The electron energy balance is the same as before [8], [9], except that a term $\mathcal{P}$ is added [given by (3)] to account for the power deposited into the plasma by the coil.

$$\frac{\partial}{\partial t}\left(\frac{3}{2}\,n_e\kappa T_e\right) + \nabla\cdot\mathbf{q}_e + e\mathbf{J}_e\cdot\mathbf{E} + 3\,\frac{m_e}{M}\,n_e\kappa\nu_m(T_e - T_g) - \mathcal{P} + \sum_j H_jR_j = 0 \tag{6}$$

with the total electron energy flux given by

$$\mathbf{q}_e = -K_e\nabla T_e + \tfrac{5}{2}\,\kappa T_e\mathbf{J}_e \tag{7}$$

where the thermal conductivity of electrons is $K_e = 3/2\kappa D_e n_e$. In (6), n_e, $\mathbf{J}_e$, and D_e are the electron density, flux, and diffusivity, respectively. T_e is the electron "temperature," T_g is the gas temperature and $\mathbf{E}$ is the electrostatic field, and κ is the Boltzmann constant. The last term on the left hand side accounts for energy loss due to all inelastic electron collisions.

C. Self-Consistent Charged Particle Transport Module

In this module, the densities of the charged particles are computed by solving the mass balance equations

$$\frac{\partial n_k}{\partial t} + \nabla\cdot\mathbf{J}_k = \sum_j R_j \tag{8}$$

where n_k and $\mathbf{J}_k$ are the density and flux, respectively, of species k. The summation in (8) is over all reactions that consume or produce species k. Neglecting convective flow, the particles fluxes are the superposition of diffusion due to concentration gradients and drift due to the presence of electric field forces. Hence $\mathbf{J}_k$ is approximated by

$$\mathbf{J}_k = -D_k\nabla n_k + q_k\mu_k n_k\mathbf{E} \tag{9}$$

where D_k, q_k, and μ_k are the diffusion coefficient, charge and mobility, respectively, of species k. Poisson's equation

$$\nabla\cdot\mathbf{E} = \frac{\rho}{\varepsilon_o} \tag{10}$$

was solved to predict the self-consistent electrostatic fields. Assuming azimuthal symmetry, this equation was solved in the (r, z) plane.

To account for the fact that ions are massive and thus do not accelerate instantaneously under the influence of an electric field, the effective field $\mathbf{E}^{eff}$ was employed

$$\frac{\partial\mathbf{E}_i^{eff}}{\partial t} = \frac{e}{\mu_i m_i}\,(\mathbf{E} - \mathbf{E}_i^{eff}) \tag{11}$$

where μ_i and m_i are the ion mobility and mass, respectively. When computing the ion flux in (8) the actual electric field was replaced by the effective electric field.

The continuity equations for all charged species and Poisson's equation were solved simultaneously. The equations were discretized in space by using the Galerkin finite element method. This resulted in a set of 9190 ordinary differential and algebraic equations which were integrated in time by a stiff integrator as before [8], [9]. The finite element mesh was chosen fine enough near the walls (cell size 35 μm) to resolve the sheaths. Since the sheath thickness in the HDP source is 100s of μ while the reactor size is 100s of mm, this introduces a severe spatial stiffness. A different approach whereby the sheath is treated separately to avoid this stiffness has also been employed [3], [5].

D. Neutral Transport and Reaction Module

This module calculates the neutral particle densities. The mass balance (8) was again used, with the distinction that the flux is only due to diffusion since the particles are neutral

$$\frac{\partial n_k^n}{\partial t} = -\nabla\cdot(-D_k^n\nabla n_k^n) + \sum_j R_j^n - \frac{n_k^n}{\tau_{res}} \tag{12}$$

where n_k^n, D_k^n, represent the density and the diffusion coefficient of the neutral species k. The summation is over all source/sink reactions that involve species k, including electron-impact as well as neutral-neutral and neutral-ion reactions. The convective flow field was not accounted for explicitly in the neutral transport and reaction module. Rather, flow losses were included through the residence time τ_{res} term in (12).

TABLE I
REACTIONS INCLUDED IN THE TWO-DIMENSIONAL ICP SIMULATION

No.	Process	Reaction	Threshold (eV)
	Electron Impact Reactions		
1	Dissociative Excitation	$Cl_2 + e \rightarrow Cl_2^*(C^1\Pi) + e \rightarrow 2Cl + e$	3.12
	Electronic Excitations (molecular)	$Cl_2 + e \rightarrow Cl_2^* + e$	
2	B^3P		2.49
3	$2^1\Pi \& 2^1\Sigma$		9.25
	Electronic Excitations (atomic)	$Cl + e \rightarrow Cl^* + e$	
4	4s		8.90
5	4p		10.40
6	3d		10.90
7	5p		11.80
8	4d		12.00
9	5d		12.40
10	Vibrational Excitation	$Cl_2 + e \rightarrow Cl_2^* + e$	0.0689
11	Molecular Ionization	$Cl_2 + e \rightarrow Cl_2^+ + 2e$	11.47
12	Atomic Ionization	$Cl + e \rightarrow Cl^+ + 2e$	12.99
13	Dissociative Attachment	$Cl_2 + e \rightarrow Cl_2^{-*} \rightarrow Cl^- + Cl$	0.0
14	Electron-Ion Neutralization	$e + Cl_2^+ \rightarrow 2Cl$	0.0
15	Electron Detachment	$e + Cl^- \rightarrow Cl + 2e$	3.61
16	Momentum Transfer (Atomic)	$e + Cl \rightarrow e + Cl$	0.0
17	Momentum Transfer (Molecular)	$e + Cl_2 \rightarrow e + Cl_2$	0.0
	Other Reactions		
18	Ion-Ion Recombination	$Cl_2^+ + Cl^- \rightarrow Cl_2 + Cl$	
19	Ion-Ion Recombination	$Cl^+ + Cl^- \rightarrow 2Cl$	
20	Volume Recombination	$Cl + Cl + M \rightarrow Cl_2 + M$	
21	Etching	$2Cl + Si \rightarrow SiCl_2$	$\gamma_{Cl \rightarrow SiCl_2} = 0.1$
		$2Cl^+ + Si \rightarrow SiCl_2$	$\gamma_{Cl^+ \rightarrow SiCl_2} = 0.5$
		$Cl_2^+ + Si \rightarrow SiCl_2$	$\gamma_{Cl_2^+ \rightarrow SiCl_2} = 0.5$
22	Wall Recombination on wafer and on non-wafer surfaces	$2Cl + Wall \rightarrow Cl_2 + Wall$	$\gamma_{Cl \rightarrow Cl_2} = 0.0082$ $\gamma_{Cl \rightarrow Cl_2} = 0.1$

TABLE II
BOUNDARY CONDITIONS USED FOR THE TWO-DIMENSIONAL ICP SIMULAITON

Quantity	Boundary Condition
n_e	$\mathbf{J}_e = \frac{1}{4}\sqrt{\frac{8\kappa T_e}{\pi m_e}} n_e \hat{\mathbf{n}} - \gamma_{Cl_2^+}\mathbf{J}_{Cl_2^+} - \gamma_{Cl^+}\mathbf{J}_{Cl^+}$
$n_{Cl_2^+}$	$\mathbf{J}_{Cl_2^+} = \mu_{Cl_2^+} n_{Cl_2^+} \mathbf{E}^{eff}_{Cl_2^+}$, if $\hat{\mathbf{n}} \bullet \mathbf{E}^{eff}_{Cl_2^+} \geq 0$ else $\mathbf{J}_{Cl_2^+} = 0$
n_{Cl^+}	$\mathbf{J}_{Cl^+} = \mu_{Cl^+} n_{Cl^+} \mathbf{E}^{eff}_{Cl^+}$, if $\hat{\mathbf{n}} \bullet \mathbf{E}^{eff}_{Cl^+} \geq 0$ else $\mathbf{J}_{Cl^+} = 0$
n_{Cl^-}	$n_{Cl^-} = 0$
T_e	$\mathbf{q}_e = \left(\frac{5}{2}\kappa T_e\right)\frac{1}{4}\sqrt{\frac{8\kappa T_e}{\pi m_e}} n_e \hat{\mathbf{n}} - \gamma_{Cl_2^+}\left(\frac{5}{2}\kappa T_{se}\right)\mathbf{J}_{Cl_2^+} - \gamma_{Cl^+}\left(\frac{5}{2}\kappa T_{se}\right)\mathbf{J}_{Cl^+}$
V	$V = 0$, on grounded surfaces and $e\mathbf{J}_{Cl_2^+} + e\mathbf{J}_{Cl^+} - e\mathbf{J}_{Cl^-} - e\mathbf{J}_e + \varepsilon_0 \frac{\partial \mathbf{E}}{\partial t} = \frac{\varepsilon_i}{d_i}\frac{\partial V_i}{\partial t}$, on the insulator
n_{Cl}	$\mathbf{J}_{Cl} = \frac{\gamma_{Cl \rightarrow Cl_2} + \gamma_{Cl \rightarrow SiCl_2}}{4}\sqrt{\frac{8\kappa T_g}{\pi m_{Cl}}} n_{Cl}\hat{\mathbf{n}} - \gamma_{Cl^+ \rightarrow Cl}\mathbf{J}_{Cl^+}$, on wafer and $\mathbf{J}_{Cl} = \frac{\gamma_{Cl \rightarrow Cl_2}}{4}\sqrt{\frac{8\kappa T_g}{\pi m_{Cl}}} n_{Cl}\hat{\mathbf{n}} - \gamma_{Cl^+ \rightarrow Cl}\mathbf{J}_{Cl^+}$, everywhere else
n_{SiCl_2}	$\mathbf{J}_{SiCl_2} = -\frac{\gamma_{Cl \rightarrow SiCl_2}}{8}\sqrt{\frac{8\kappa T_g}{\pi m_{Cl}}} n_{Cl}\hat{\mathbf{n}} - \frac{\gamma_{Cl^+ \rightarrow SiCl_2}}{2}\mathbf{J}_{Cl^+} - \gamma_{Cl_2^+ \rightarrow SiCl_2}\mathbf{J}_{Cl_2^+}$, on wafer and $\nabla n_{SiCl_2} = 0$ everywhere else

Note: ε_i, d_i and V_i are the dielectric constant, thickness and voltage drop across the insulator.

Since the neutral species module does not exhibit any "stiffness" in space (or time) a coarser spatial discretization grid, compared to the one used for the charged particle modules, was employed for neutrals.

E. Chemistry

Etching of polysilicon with pure chlorine gas was studied. The reaction set, shown in Table I, is an augmented version of that used before [10]. In particular, detachment of negative ions by electron collisions (process #15) and the etching reactions (#21) were added. The etching product $SiCl_2$ was assumed to form by atomic chlorine reacting on the wafer with a probability $\gamma_{Cl \rightarrow SiCl_2}$ of 0.1, and by atomic and molecular chlorine ions reacting on the wafer with probabilities $\gamma_{Cl^+ \rightarrow SiCl_2}$ and $\gamma_{Cl_2^+ \rightarrow SiCl_2}$ respectively, both equal to 0.5 [11]. Also, chlorine radicals were assumed to recombine on the reactor walls with a probability of $\gamma_{Cl \rightarrow Cl_2}$ 0.1, and on the wafer with a probability $\gamma_{Cl \rightarrow Cl_2}$ of 0.0082 to yield Cl_2. The surface neutralization probability for atomic $\gamma_{Cl^+ \rightarrow Cl}$ and molecular chlorine ions $\gamma_{Cl_2^+ \rightarrow Cl_2}$ was set equal to 0.5 on the wafer and 1.0 on all other walls.

For the results shown below a Maxwellian electron energy distribution function (EEDF) was assumed. The electron-impact rate coefficients k_j were calculated from the known cross-sections $\sigma_j(\varepsilon)$ using the expression

$$k_j = \int_0^\infty \sigma_j(\varepsilon) u(\varepsilon) f_M(\varepsilon)\, d\varepsilon \tag{13}$$

where $u(\varepsilon)$ is the electron velocity, ε is the electron energy and $f_M(\varepsilon)$ is the Maxwellian EEDF. Using (13), the rate coefficients were expressed as a function of the electron temperature, which is one of the unknowns [see (6)]. In practice, look up tables were used to interpolate the rate coefficients. Other options to determine the EEDF include a 0-D Boltzmann solver as before [8], or a 2-D Monte Carlo solver [5].

For the pure Cl_2 inlet gas, the species considered in the model were e, Cl_2^+, Cl^+, Cl^-, Cl, and $SiCl_2$. The ion mobilties were computed from constant cross-sections obtained from [12]. The mobilities used in this simulation are $\mu N = 5.62\times10^{19}, 6.48\times10^{19}, 6.48\times10^{19}$ (cm V s)$^{-1}$ for Cl_2^+, Cl^+, and Cl^- respectively, where N is the total gas density. The electron mobility was computed from the collision frequency $\nu_e(\mathbf{x}, t) = \sum_j k_j n_j$ where the summation is over all electron-impact reactions and k_j, n_j, represent the rate coefficient and the density of the species associated with the jth reaction, respectively. The charged particle diffusion coefficients were obtained from the mobilities using Einstein's relation $D_k = \mu_k \kappa T_k / q_k$, where κ is the Boltzmann constant. The temperature T_k of the ions was assumed constant and equal to 0.12 eV. The diffusion coefficients for neutral species were obtained by using the standard Chapman-Enskog kinetic theory, based on the Lennard Jones parameters of [12]. The diffusion coefficients used for Cl, and $SiCl_2$ were $DN = 6.21 \times 10^{18}$ and 2.36×10^{18} (cm s)$^{-1}$, respectively.

F. Boundary Conditions

The boundary conditions are listed in Table II. The electron flux was set equal to the thermal flux perpendicular to the walls minus the secondary electron flux due to positive ion (Cl_2^+, Cl^+) bombardment. For this simulation, the secondary electron coefficient was set equal to zero ($\gamma_{Cl_2^+} = \gamma_{Cl^+} = 0$). For the positive ions, the flux on the walls was only due to drift under the electric field. Since negative ions are repelled by the sheath, the density of Cl^- on the walls was set equal to zero. The electron energy flux on the walls was deduced from the corresponding electron density flux (T_{se} is the temperature of the secondary electrons). The potential on grounded walls was zero, while that on the quartz insulator was determined as

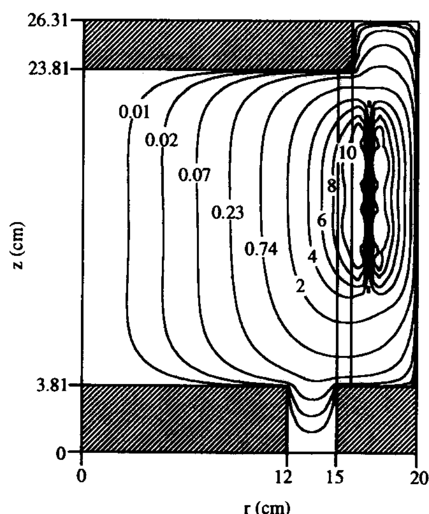

Fig. 3. Amplitude of the azimuthal electric field (V/cm) produced by the coil. Base case conditions.

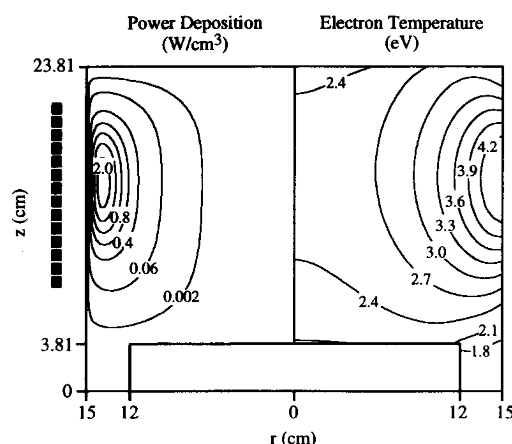

Fig. 4. Power deposition (left) and electron temperature (right) profiles in the reactor. Base case conditions.

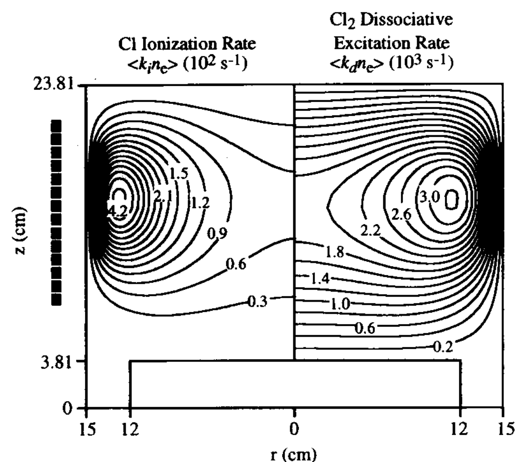

Fig. 5. Atomic chlorine ionization (left) and molecular chlorine dissociative excitation (right) rates. Base case conditions.

part of the solution using a current boundary condition. The net flux of Cl atoms at the wafer surface equals the thermal flux times the sum of the recombination and etching reaction probabilities, minus the neutralization flux of atomic chlorine ions. A similar boundary condition was applied to the rest of the reactor walls where no etching occurs. Note that $\gamma_{Cl^+ \rightarrow Cl}$ is 0.5 on the wafer and 1.0 on all other walls. The flux of $SiCl_2$ out of the wafer is due to etching by Cl atoms and Cl^+ and Cl_2^+ ions. The gradient of the $SiCl_2$ density was set equal to zero on walls other than the wafer. Although $SiCl_2$ may stick on the walls depositing silicon, this silicon can be reetched by Cl atoms in the plasma; at steady-state the net deposition rate should be zero.

The system was constrained by the total number density assumed constant as a function of position. The presence of negative ions slows down convergence to a steady-state solution, since the time scale of negative ion reactions is long. An acceleration scheme may be used to speed-up convergence [5], [8].

III. Results and Discussion

The following conditions were chosen as a base case: total pressure 10 mtorr, plasma power 3560 W, frequency 13.56 MHz, gas temperature 500 K, feed gas flow rate 200 sccm of pure chlorine. In discussing the figures below, the base case values were used unless noted otherwise.

The amplitude of the azimuthal electric field (in V/cm) is shown in Fig. 3. The field penetrates the quartz enclosure but not the metal structures. The field decays by an order of magnitude within several cm into the high density plasma. The grid for solving Maxwell's equations is not fine enough to resolve the coil structure accurately. Also, since the metallic walls are relatively far from the coils, most of the power is deposited in the plasma. The power deposition profiles are seen in Fig. 4 (left). Most of the power is deposited near the coil, since the electromagnetic wave can not penetrate the high density plasma for more than a few skin depths (compare to Fig. 3). The peak power deposition is greater than 2 W/cm^3; when averaged over the reactor volume the power deposition becomes 0.24 W/cm^3. The electron temperature distribution is shown in Fig. 4 (right). Although the power is deposited only over a narrow zone, thermal conduction at the low operating pressure helps in heating up the whole plasma. The electron temperature is highest near the coil where the power deposited per electron is highest. The electrons cool down substantially in the narrow annular region between the substrate platen and the metal outer wall ($12 < r < 15$ cm, $0 < z < 3.81$ cm). Higher pressures tend to produce larger electron temperature variations. Lower pressures tend to increase the electron thermal conductivity thus making the electron energy less nonuniform.

The resulting rates of dissociative excitation of molecular chlorine (reaction 1, Table I) and ionization of atomic chlorine (reaction 12, Table I) are shown in Fig. 5. The spatial distribution of the ionization rate coefficient ($k_i n_e$) is more nonuniform compared to the dissociation rate coefficient ($k_d n_e$) because of the larger threshold of the former process. Interestingly, even though the power is deposited very near the coil (Fig. 4), the electron-impact reaction rates are fairly high even in the reactor centerline. This testifies to the "nonlocal" nature of the system; electrons heated in the high electric field region near the coil can carry their energy and do chemistry large distances away. This nonlocal feature of the electrons is expected to be more important as pressure decreases.

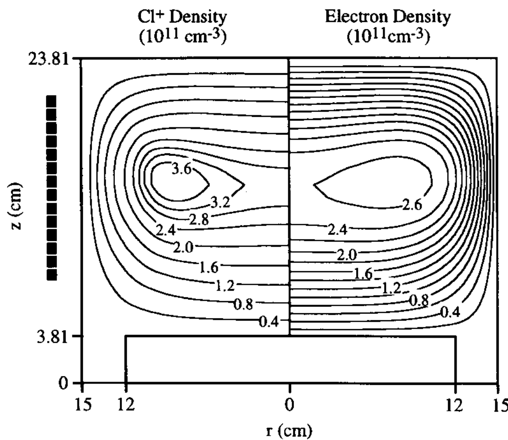

Fig. 6. Atomic chlorine ion (left) and electron (right) density distributions. Base case conditions.

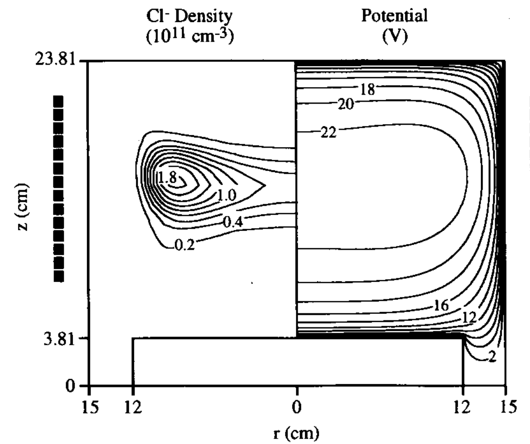

Fig. 7. Negative ion (left) and electrostatic potential (right) distributions. Base case conditions.

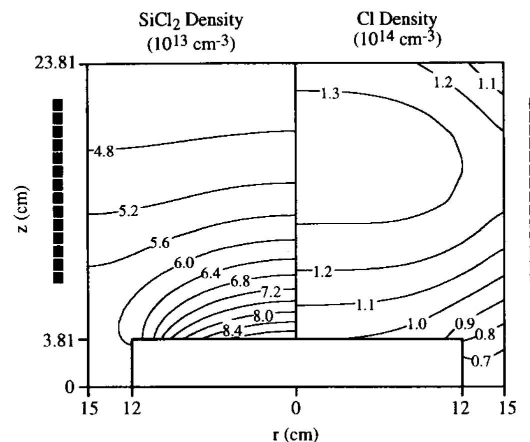

Fig. 8. Silicon dichloride product (left) and atomic chlorine density (right) distributions. Base case conditions.

The majority positive ion (Cl^+) and electron density distributions are shown in Fig. 6. The peak ion density is nearly 4×10^{11} cm^{-3}. An off axis maximum in the densities is observed which is further away from the coil compared to the ionization maximum. The charged species densities decay rapidly toward the walls. However, in contrast to the low plasma density capacitively coupled reactors, the electron density is quite high even very near the wall. This is because the sheaths are thin due to the small (10s of μ) Debye length and the absence of high voltages across the sheath. The density gradients are steeper near the radial wall in the power deposition zone. Interestingly, the radial ion density profile changes from one with an off-axis peak near the middle of the reactor to one with an on-axis peak near the wafer. In general, the positive ion spatial density profile depends on the values of power deposition, pressure, and reactor aspect ratio (radius/height). High values of these quantities favor off axis maxima, low values favor maxima on axis.

The Cl^- negative ion density and potential distribution are depicted in Fig. 7. Negative ions are expelled from the plasma sheath and pool in the bulk in regions of high potential. The negative ion losses are purely by gas-phase reactions including ion-ion recombination (reactions #18 and 19 in Table I) and detachment by electron collisions (reaction #15). The discharge is moderately electronegative in the sense that the peak negative ion density is comparable to the electron density in the bulk plasma. The ratio of negative ion to electron density is much lower than that in high pressure low plasma density discharges [9]. This is because Cl_2 is highly dissociated, and electron attachment to Cl atoms is unfavorable. It is interesting to note that the negative ion density is very low near the walls, compared to the electron density; It is conceivable that the ion motion in the presheath is not affected by the negative ions, i.e., despite the fact that the discharge is electronegative, the sheath can be treated as one in an electropositive discharge (which affords a simplified treatment). A separate treatment of the sheath may be advantageous because of the extreme spatial stiffness of the system. The potential distribution shown on the right of Fig. 7 reinforces the notion of spatial stiffness. The potential gradients are extremely high in the sheath formed over the walls. The peak plasma potential is some 23 V under these conditions. Also it is noted that the electron density peaks at the same location as the potential.

The Cl atom density profiles are shown in Fig. 8 (right). Concentration gradients are still evident despite the low operating pressure. The Cl atom density is lower near the wafer because of the etching reaction and the product (silicon chloride) evolution from the wafer which "displaces" Cl (remember that the total number density was constrained to be constant as a function of position). Although Cl atoms are produced mainly at large radii (Fig. 5, right) diffusion fills in the region near the reactor center. Gas-phase losses of Cl are small under the low operating pressures; so unless there is a strong loss of atoms (by wall recombination or etching) along the axial walls as the atoms diffuse radially inwards, the Cl atom density will be maximum at the center. Wall losses depend critically on the reaction probability but also on the surface to volume ratio. Low aspect ratio (radius/height) tall reactors are more likely to produce a peak on axis. High aspect ratio squat reactors are more likely to produce a peak off axis; the peak location will be closer to the position of maximum generation rate for higher aspect ratios. The surface to volume ratio effect can also be seen in Fig. 8. The Cl atom density at the upper right hand corner is lower due to more wall recombination in that area; the same holds true in the annular zone between the substrate platen and the outer wall

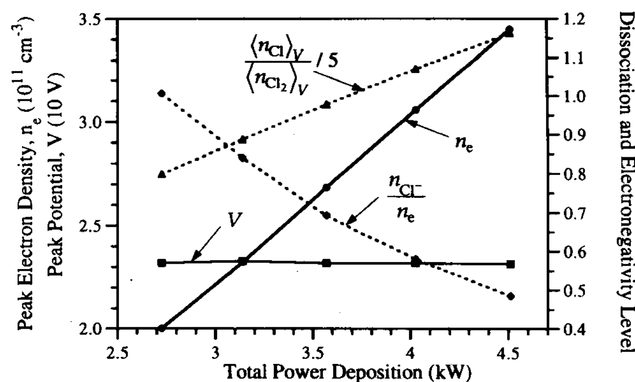

Fig. 9. Peak electron density and plasma potential (solid lines, left axis), and ratio of peak negative ion to electron density and ratio of (volume-averaged) Cl to Cl_2 neutral species density (dotted lines, right axis). The Cl to Cl_2 density ratio has been divided by 5 to fit on the scale of the right axis. Points are calculated quantities, lines are drawn to guide the eye.

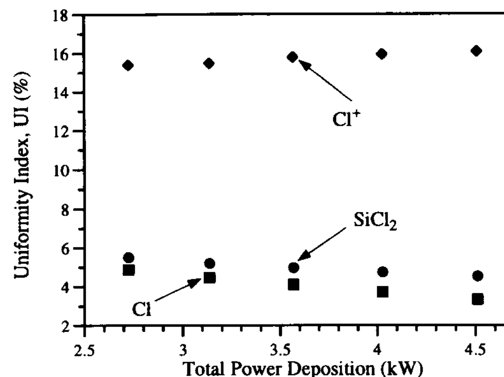

Fig. 10. Uniformity index of Cl^+ ion, Cl radical, and $SiCl_2$ molecule density as a function of power into the plasma. The uniformity index is defined as UI=(Max-Min)/(2 × Avg), where Max, Min, and Avg are the maximum, minimum and (radially) averaged value of the respective quantity. Points are calculated values.

of the reactor. The profile shown in Fig. 8 does not account for the effects of gas flow (i.e., it was calculated based on purely diffusive transport). Flow may modify the species gradients, depending on the reactor design, pressure and flow rate.

The $SiCl_2$ molecule density is also shown in Fig. 8 (left). This is a bigger species (compared to Cl) and its diffusivity is correspondingly smaller. Also, there is a localized source of product at the wafer surface. These facts combine to produce a fairly nonuniform product distribution in the reactor. Despite the low operating pressure, concentrations differ by 50% between the wafer and the reactor upper wall. As expected, the product density decays smoothly away from the wafer source. Product ionization was not accounted for in the present calculation simply because the electron collision cross-sections are not available. Fig. 8 shows that the product density can build up to be a substantial fraction of the total gas density. Clearly, electron impact reactions with silicon chlorides can make a difference. There is a need for cross-section data for collisions involving atoms and radicals resulting not only from the feedstock gas but also from the reaction products. This need is more acute in low pressure high density plasmas where the degree of dissociation of different species is normally much greater than that in high pressure low density plasmas.

The effect of power deposited in the plasma on several key plasma quantities is shown in Fig. 9. The electron density increases linearly with power, which has been observed experimentally in HDP systems [13]. The plasma potential is independent of power deposition. The ratio of peak negative ion to electron density drops with increasing power which suggests that the plasma electronegativity decreases. This is due to more dissociation of molecular chlorine as power increases, as shown by the ratio of the (volume-averaged) Cl and Cl_2 neutral species densities.

One of the most important features that reactor designs are striving to achieve is radical and ion flux uniformity across large diameter wafers. The uniformity of the Cl^+ ion, Cl radical, and $SiCl_2$ molecule densities over a 200 mm-diameter wafer are shown in Fig. 10 as a function of power deposited in the plasma. The uniformity index is defined as UI=(Max-Min)/(2× Avg), where Max, Min, and Avg are the maximum, minimum, and (radially) averaged value of the

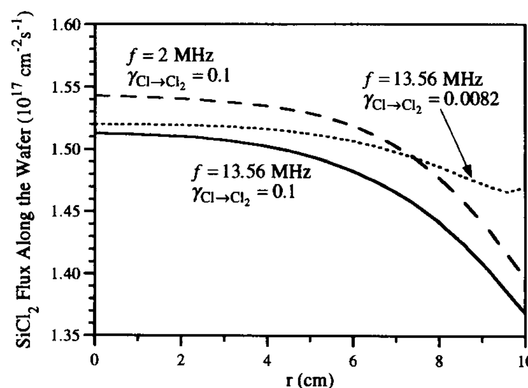

Fig. 11. $SiCl_2$ product flux along the wafer radius. A flux of 10^{17} $SiCl_2$ molecules/cm^2-s corresponds to an etch rate of 1.2 μ/min. Solid line is for the base case conditions. Dashed line is for the base case except that the coil excitation frequency is 2 MHz. Dotted line is for the base case except that the Cl radical recombination probability on the ring surface surrounding the wafer is 0.0082.

respective quantity. The lower the value of UI, the better the uniformity. Fig. 10 clearly shows that the Cl radical uniformity is much better than the Cl^+ ion uniformity. The ion uniformity becomes slightly worse while the radical uniformity improves as the power increases. The UI of the reaction product $SiCl_2$ follows the trend of the Cl radical uniformity since under these conditions etching is dominated by radicals.

The product flux distribution (proportional to the etch rate) along the wafer radius is shown in Fig. 11 for three different cases. A flux of 10^{17} $SiCl_2$ molecules/cm^2-s corresponds to an etch rate of 1.2 μ/min. The solid line is for the base case conditions: 13.56 MHz coil excitation frequency and the Cl radicals recombine on all nonwafer surfaces with probability $\gamma = 0.1$ to yield Cl_2. The result of keeping the same wall recombination probability for Cl but changing the coil excitation frequency to 2 MHz is shown by the dashed line. The etch uniformity is not affected greatly under these conditions. The dotted line shows the case of 13.56 MHz coil frequency, but the Cl recombination probability on the ring surface surrounding the wafer (10 cm $< r <$ 12 cm) is now $\gamma = 0.0082$ (keeping $\gamma = 0.1$ on all other nonwafer surfaces). The etch uniformity is greatly improved. Under the base case conditions, the Cl radical density is highest at the

wafer center and lowest at the edge (see Fig. 8). When the surface surrounding the wafer is not as reactive against Cl, the radical concentration builds up near the wafer edge alleviating the concentration gradient. For the conditions examined here, etching by Cl is dominant; hence an improvement in the Cl radial density profile leads to better uniformity. This local loading effect is well understood and has been studied in connection with high pressure (100s of mtorr) capacitively studied systems [14]. One may at first think that due to the high species diffusivities at the low operating pressures of HDP sources, loading may not be important. However, one should bare in mind that it is the relative importance of diffusion as compared to the surface reaction that determines the severity of the concentration gradient (so called Thiele Modulus, see [14]). Even if diffusion is fast, concentration gradients will build up if the surface reaction is faster. Of course, the etch uniformity also depends on the relative importance of chemical versus ion-assisted etching. For example, under conditions of etching being dominated by ions (e.g., undoped poly), the uniformity would be worse than that shown in Fig. 11, for the system studied (see UI for ions in Fig. 10).

It should be noted the Cl^+ flux on the wafer has a maximum on axis despite the fact that an off axis maximum in the Cl^+ density exists further away from the wafer. The flux of Cl_2^+ bombarding the wafer on the other hand was found to have a maximum at the wafer edge. However, under the conditions of high gas dissociation examined, the molecular ion density was one order of magnitude lower than the atomic ion density, and did not contribute significantly to etching.

IV. Summary

A two-dimensional simulation of polysilicon etching with chlorine in an inductively coupled high density plasma source was developed based on the fluid approximation. A modular approach was used to couple the disparate time scales of plasma and neutral transport in a self-consistent manner. This allowed a fairly complex plasma chemistry (among electrons, ions and neutrals) to be included in the simulation. The electromagnetic wave emanating from the solenoidal coil was absorbed in the high density plasma within a few cm from the cylindrical quartz wall. The spatial distribution of ions and neutrals over the wafer is a complex function of mainly power, pressure and reactor aspect ratio. The radial uniformity of the Cl atom flux was better than that of the ion flux. The neutral density distribution was also affected by the reactivity of the wafer as compared to that of the surrounding electrode. Such a local loading effect manifested itself even at the low pressure of 10 mtorr examined. As power deposition was increased, the electron density increased linearly, the plasma became less electronegative, the degree of gas dissociation increased, and the plasma potential remained constant.

The simulation code can be used to do further parametric investigations of the effect of plasma reactor and coil design and operating conditions on the degree of gas dissociation, plasma electronegativity, and plasma uniformity across large diameter wafers. Capacitive coupling from the antenna coil and any RF bias of the substrate can be handled readily in a manner similar to capacitively-coupled reactors [8], [9]. Extending the simulation to include these cases, and comparison with experimental data are the subject of continuing work. Comparison with experiments in well defined geometries [13] is particularly important and is left as future work.

Acknowledgment

The authors thank Prof. M. Kushner of the University of Illinois for sharing with us collision cross-sections for ions and neutrals. They also thank M. Surendra of IBM, V. Donnelly of AT&T Bell Laboratories, and P. Miller of SNLA for sending them preprints of their work prior to publication.

References

[1] M. A. Lieberman and R. A. Gottscho, "Design of high density plasma sources for materials processing," in *Physics of Thin Films,* M. Francombe and J. Vossen, Eds. Orlando, FL: Academic, 1993.

[2] K. Tsujimoto, T. Kumihashi, N. Kofuji, and S. Tachi, "Short-gas-residence-time ECR plasma etching," *J. Vac. Sci. Technol. A,* vol. 12, pp. 1209–1215, 1994.

[3] R. A. Stewart, P. Vitello, and D. B. Graves, "Two-dimensional fluid model of high density inductively coupled plasma sources," *J. Vac. Sci. Technol. B,* vol. 12, pp. 478–485, 1994.

[4] A. A. Paranjpe, "Modeling an inductively coupled plasma source," *J. Vac. Sci. Technol., A,* vol. 12, no. 4, pp. 1221–1228, 1994.

[5] P. L. G. Ventzek, R. J. Hoekstra, and M. J. Kushner, "Two-dimensional modeling of high plasma density inductively coupled sources for materials processing," *J. Vac. Sci. Technol. B,* vol. 12, pp. 461–477, 1994.

[6] D. P. Lymberopoulos and D. J. Economou, "Modeling and simulation of inductively coupled high density plasma sources," in *Proc. 10th Plasma Processing Symp.,* G. S. Mathad and D. W. Hess, Eds., 1994, vol. 94–20, pp. 1–12.

[7] M. Surendra, "Radiofrequency discharge benchmark model comparison," *Plasma Sources Sci. Technol.,* to appear

[8] D. P. Lymberopoulos and D. J. Economou, "Fluid simulations of glow discharges: Effect of metastable atoms in argon," *Appl. Phys. Lett.,* vol. 63, pp. 2478–2480, 1993.

[9] ——, "Modeling and simulation of glow discharge plasma reactors," *J. Vac. Sci. Technol. A,* vol. 12, no. 4, pp. 1229–1236, 1994.

[10] S. C. Deshmukh and D. J. Economou, "Remote plasma etching reactors: Modeling and experiment," *J. Vac. Sci. Technol. B,* vol. 11, pp. 206–215, 1993.

[11] C. C. Cheng, K. V. Guinn, V. M. Donnelly, and I. P. Herman, "*In-situ* pulsed laser-induced desorption studies of the silicon chloride surface layer during silicon etching in high density plasmas of Cl_2 and Cl_2/O_2 mixtures," *J. Vac. Sci. Technol. A,* vol. 12, pp. 2630–2640, 1994.

[12] M. J. Kushner, personal communication.

[13] P. A. Miller, G. A. Hebner, K. E. Greenberg, P. D. Pochan, and B. P. Aragon, "An inductively coupled plasma source for the GEC RF Reference Cell," *J. Res. Nat. Inst. Standards Technol.,* 1995.

[14] D. J. Economou, S.-K. Park, and G. Williams, "Uniformity of etching in parallel plate plasma reactors," *J. Electrochem. Soc.,* vol. 136, pp. 188–198, 1989.

Dimitris P. Lymberopoulos received the B.S. degree in chemical engineering at the University of Patras, Greece. He is pursuing the Ph.D. degree at the University of Houston, Houston, TX.

Demetre J. Economou, for a photograph and biography, see this issue, p. 502.